

pubs.acs.org/cm Article

# Halide-Mediated Phase Control of $Fe_xCo_{1-x}C_y$ Nanoparticles

Isabella Bertini, Bipin Lamichhane, Samantha Bell, Keyou Mao, Shyam Kattel,\* and Geoffrey Strouse\*



Cite This: https://doi.org/10.1021/acs.chemmater.4c00701



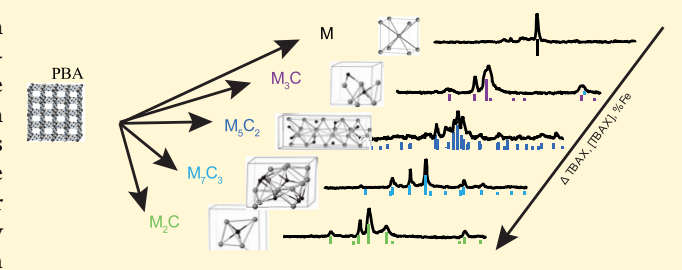
**ACCESS** I

Metrics & More

Article Recommendations

Supporting Information

**ABSTRACT:** The ability to control the compositional phase in first row transition metal bimetallic carbides as well as systematically controlling the metal ratio is complicated by the rich phase diagram, differences in metal reactivity, and differences in carbon solubility in the first-row metal carbides. Prussian blue analogues (PBAs) have been shown to act as a single source precursor for the formation of nanocrystal metal carbides with maintenance of their metal. An investigation of crystal phase control in the ternary  $(Fe_xCo_{1-x})_yC_z$  formed by PBA collapse is yet to be explored. In



this study, we demonstrate the ability to tune phase (from most carbon rich to least carbon rich)  $M_2C$ ,  $M_5C_2$ ,  $M_7C_3$ , and  $M_3C$ , as well as the bimetallic alloy (M) in bimetallic FeCo nanocarbides through a strategy that pairs synthetic and density functional theory approaches to enable future targeted structure—function research on intriguing catalytic, therapeutic, and magnetic applications.

# INTRODUCTION

Following from the scientific dogma of "form follows function", to obtain a desired property, the structure of a material dictates its potential uses. First row transition metal carbides possess rich phase diagrams, 1-5 where the structure and carbon content strongly influence the materials properties, reflecting changes in orbital interactions and subsequent band structure. In the catalytic literature, it is known that chemical activity is dependent on phase (anatase vs rutile TiO<sub>2</sub> for instance) or as observed in Fischer-Tropsch catalysis, the Hagg carbide  $(Fe_5C_2)$  is more catalytically active than other  $M_xC_y$  carbides Likewise, the presence of synergistic effects in ternary systems (i.e., FeCoP, FeCoO, and FeCoC) has suggested that ternary or higher entropy materials may be better catalysts if the structural phase of a material is controlled. 13-21 In ternary systems such as bimetallic carbides, the reaction phase space naturally becomes more complex; therefore, the number of possible materials isolable increases.

Whether the goal is to prepare hardened materials, corrosion resistant, or improve catalytic activity, developing synthetic methods to isolate a specific compositional and structural phase from a reaction mixture is crucial. 12,22–25 When materials are grown via solid state methods, temperature and stoichiometry are employed to provide phase control; however, when grown as nanomaterials through solvent based methods, chemical control is strongly impacted by the thermodynamic and kinetic steps involved in nucleation and growth. As a result, being able to isolate a specific composition and structure is extremely difficult. 26–28

A material system that exhibits a rich phase diagram, is known to have properties dependent on structure and composition, <sup>29</sup> and is of immense interest in catalysis, as well as metallurgy, is the first row metal carbides. <sup>3,30,31</sup> The

performance of the metal carbides is directly dependent on metal composition and crystallographic phase, particularly in the case of binary systems where synergistic effects have been hypothesized.<sup>7,32–36</sup> The bimetallic FeCoC ternary system has been identified as a promising material for catalytic, diagnostic imaging,<sup>22</sup> data storage,<sup>37,38</sup> and environmental remediation applications.<sup>39</sup> Although Fe and Co carbide materials are considered "ancient advance materials",<sup>23,24</sup> there has been limited research on the use of synthetic parameters to prepare unique crystal phases.

Instead of focusing on the isolation of several different phases, most studies have investigated properties of the mixed phase or the one pure phase material isolable. Development of synthetic methods that allow careful control of the bimetallic composition in a specific crystallographic phase is challenging for FeCoC as the phase diagram of FeC possesses a rich phase space. To date, monometallic carbides remain the only carbides whose structures have been thoroughly studied. The most common Fe carbide phases are Fe<sub>3</sub>C and Fe<sub>7</sub>C<sub>3</sub>, while cobalt carbide prefers to crystallize in the Co<sub>3</sub>C or Co<sub>2</sub>C phase. Many other phases of iron carbides exist (FeC, Fe<sub>2</sub>C, Fe<sub>3</sub>C, Fe<sub>3</sub>C<sub>2</sub>, Fe<sub>4</sub>C, Fe<sub>5</sub>C<sub>2</sub>, Fe<sub>6</sub>C, Fe<sub>7</sub>C<sub>3</sub>, Fe<sub>8</sub>C, Fe<sub>2</sub>C<sub>9</sub>, and Fe<sub>23</sub>C<sub>6</sub>) that are said to be metastable phases. <sup>12,40</sup> The ternary Fe—Co—C phase diagram describes only the bimetallic alloy which packs in two crystal structures (FCC and BCC) and once the carbon wt % reaches 4%, the carbon crystallizes separately

Received: March 14, 2024 Revised: August 6, 2024 Accepted: August 7, 2024



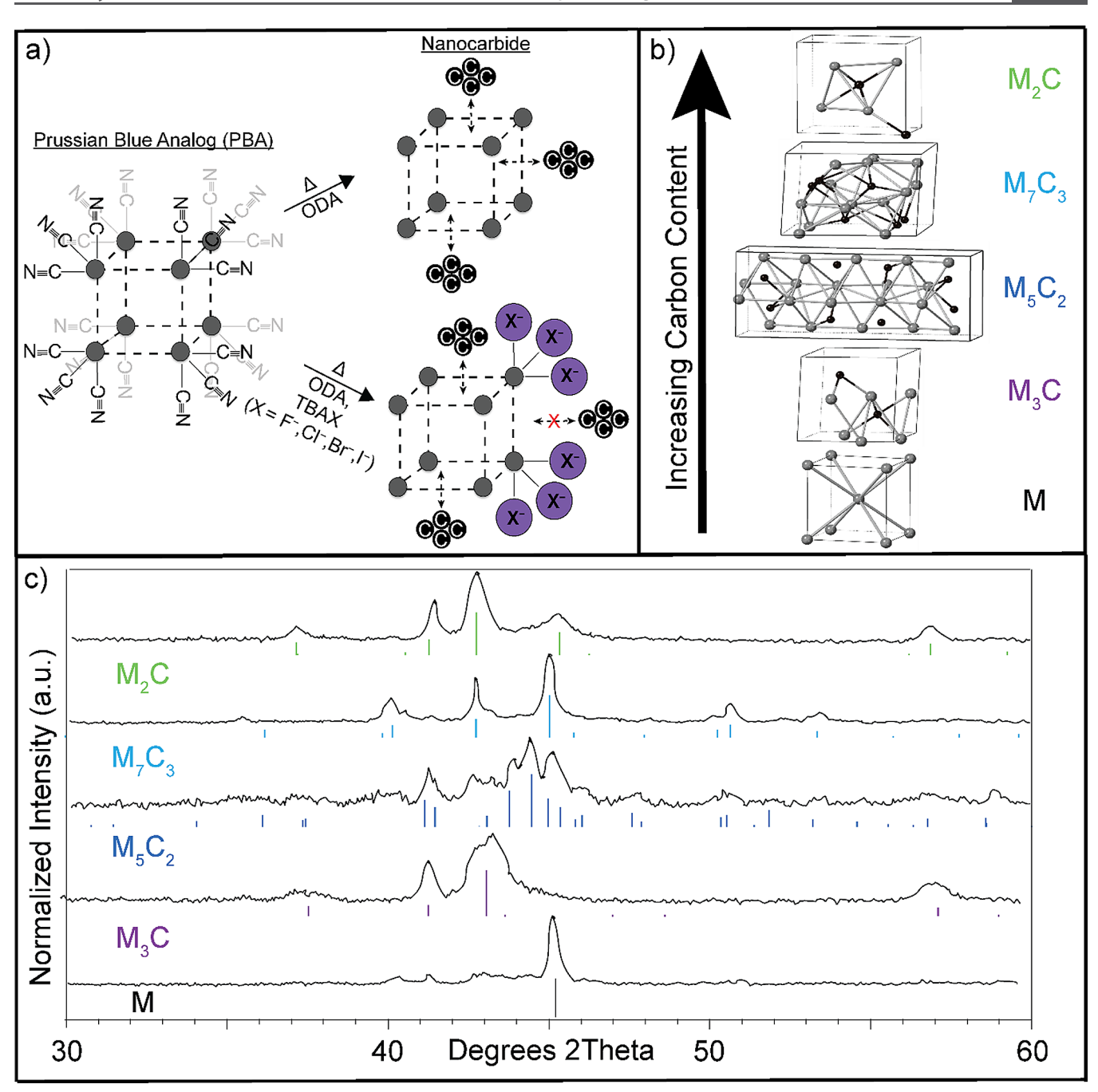


Figure 1. (a) Schematic for the thermal conversion of mesocrystal Fe/Co PBA to nanocrystal  $M_xC_y$  in the presence of octadecylamine (ODA) and TBAX (X = F, Cl, Br, I). (b) Thermodynamically stable  $M_xC_y$  phases for the (Fe<sub>x</sub>Co<sub>1-x</sub>)<sub>y</sub>C<sub>z</sub> system. (c) Selected pXRD of isolated pure phase  $M_xC_y$  nanocrystals with reference patterns for phase assignment. Green represents the  $M_2C$  phase (COD: 1528415), light blue represents the  $M_7C_3$  phase (ICSD: 76830), dark blue represents the  $M_7C_9$  phase (ICSD: 423885), purple represents the  $M_7C_9$  phase (ICSD: 42542), and black represents the M FeCo metal alloy (ICSD: 102381).

from the metal as graphitic carbon. 1,3 Despite the reported strategies for synthesizing Fe and Co carbide monometallic materials, 37,41–43 it is widely accepted that high-temperature colloidal synthesis from chemical precursors provides the most control of nanomaterial phase, crystallinity, and size. 23 The formation of nanometal carbides from solvothermal decomposition of molecular precursors, such as  $M(CO)_x^{44,45}$  and  $M(CO_3)_x^{46}$  carburization of  $MO_x^{47}$  and from Prussian blue analogue (PBA)2,21,28,48 decomposition has been reported in the literature; however, the resultant materials exhibit mixed  $M_xC_y$  phase composition.

In monometallic nanocarbides, it has been reported that addition of halide salts leads to isolation of single phase Fe<sub>2</sub>C, Fe<sub>5</sub>C<sub>2</sub>, Fe<sub>7</sub>C<sub>3</sub>, and Fe<sub>3</sub>C and for cobalt Co<sub>3</sub>C and Co<sub>2</sub>C, depending on the reaction conditions. It is reasonable to assume that halide binding to the monomer or to the growing carbide nanofacet will be unique to each halide species and to the metal. Ma and co-workers investigated synthetic control in the Hagg carbide (Fe<sub>5</sub>C<sub>2</sub>) using bromide ions, where it was observed that the addition of bromide ion allowed selective isolation of the Fe<sub>5</sub>C<sub>2</sub> phase instead of Fe<sub>3</sub>C (thermodynamically most stable). The use of chloride ions was reported by

Table 1. Synthetic Parameters for the Isolation of the Pure Phase Materials<sup>a</sup>

isolated FeCoC phase	ref card	TBAX	[TBAX] (mmol)	time (h)	temp (°C)	% Fe initial	% Fe final
M <sub>3</sub> C	ICSD:42542	TBAC	0.1	1	350	60	60
$M_2C$	ICSD:423885	TBAC	0.5	1	350	19	16
$M_2C$	COD:1528415	TBAC	1	1	350	19	10
$M_2C$	COD:1528415	TBAC	2	1	350	19	8
$M_2C$	COD:1528415	TBAC	2	1	350	35	13
$M_7C_3$	ICSD:76830	TBAC	3	1	350	80	72
$M_2C$	COD:1528415	TBAB	0.5	1	350	19	14
$M_2C$	COD:1528415	TBAB	1	1	350	19	7
$M_2C$	COD:1528415	TBAB	1	1	350	35	11
$M_2C$	COD:1528415	TBAB	2	1	350	19	5
$M_2C$	COD:1528415	TBAB	3	1	350	19	3
M	ICSD:102381	TBAB	3	1	350	35	3
M	ICSD:102381	TBAB	3	1	350	80	28
$M_2C$	COD:1528415	TBAI	0.5	1	350	19	10
$M_2C$	COD:1528415	TBAI	0.5	1	350	35	26
M	ICSD:102381	TBAI	3	1	350	19	4
M	ICSD:102381	TBAI	3	1	350	35	9
M	ICSD:102381	TBAI	3	1	350	60	11
$M_5C_2$	ICSD:423885	TBAI	3	1	350	80	35

"Initial % Fe reflects the XRF ratio for the PBA precursor and the final % Fe reflects the XRF ratio for the carbide.

Carpenter and co-workers <sup>46</sup> to allow  $Fe_7C_3$  and  $Fe_3C$  isolation, <sup>1</sup> while Gao and co-workers used chlorides to isolate  $Fe_2C$ ,  $Fe_3C$ , and  $Fe_3C_2$ . <sup>49</sup> Both Ma and Carpenter expanded the use of halides by demonstrating selective isolation of  $Co_2C$  instead of  $Co_3C$ . <sup>45</sup> The control of  $Fe_xC_y$  phase by addition of halide ions was attributed to bonding of the Fe to the halide through via Bader charge analysis. <sup>49</sup> While the role of halide salts on phase control is widely believed to reflect control of monomer activity, no comparative study of halide species has been performed, nor have bimetallic carbides been investigated, where phase control is more complex. Furthermore, halide mediated synthesis has not yet been translated to the ternary  $(Fe_xCo_{1-x})_vC_z$  system.

Herein, we investigate the effect of halides on the isolation of pure phase bimetallic FeCo nanocarbides  $(Fe_xCo_{1-x})_yC_z$ through the pairing of experimental and computational strategies to further elucidate the mechanism of systematic synthetic control. The results of the study cleanly delineate regions of phase stability for Fe:Co metal ratios under selective halide concentrations. The impact of changing the halide salt, its concentration, and the metal ratio on conversion to a carbide phase was investigated. Density functional theory (DFT) calculations performed on the addition of carbon in the presence of the alkylamine at FeCo (110) facet allowed the competitive binding of the halide to the surface to be evaluated. The energetics from DFT provide a model where C diffusion in and out of the nanocarbide is controlled by surface stabilization. The observations in the nanocarbide synthesis via a thermal decomposition of a PBA provides a strategy to control of phase in a broader class of materials known as MX-ides (oxides, sulfides, selenides, phosphides, and nitrides). The ability to isolate bimetallic carbides of discrete phases and potentially apply the strategy to multimetallic carbides could provide a means for the catalytic community to test the hypothesis that catalytic performance is dependent on crystal structure and material composition for high-value multimetallic MX-ide families.

# RESULTS

As shown schematically in Figure 1a, a set of high temperature solution collapses of Fe:Co PBAs were carried out in the presence of tetrabutyl ammonium halides (TBAX, where X = F<sup>-</sup>, Cl<sup>-</sup>, Br<sup>-</sup>, and I<sup>-</sup>). The reaction details are provided in Supporting Information Table S1. The systematic evaluation of TBAX concentration at various Fe:Co metal ratios on the phase isolation of the carbide and the change in metal ion ratio for the isolated carbide following thermal conversion of bimetallic Fe:Co PBAs provides insight into the ability to target composition and structural phase. All reactions were carried out for 1 h in boiling octadecylamine (ODA) under N2 to avoid oxide formation. The ratio of Fe to Co in the bimetallic PBAs were prepared by addition of controlled ratios of M(II) chloride to M(III) cyanometallate salts of Fe and Co to ensure Fe:Co composition, as previously described.<sup>21</sup> The PBA starting size is Fe:Co ratio dependent and ranged from 50 to 150 nm with a 20% size distribution (SEM images and XRF compositional details are available in Supporting Information Figures S1 and S2). Isolation of the nanocarbide from the reaction is accomplished by centrifugation followed by magnetic separation from a toluene solution (XRF ratios for all resultant nanocarbides are reported in Supporting Information Table S1).

In Figure 1b, the  $M_xC_y$  nanocarbide crystal phases for Fe and Co carbides that can form are shown. The isolated phases for each reaction condition are evaluated by the whole pattern fitting of the pXRD patterns available in Supporting Information Figure S3. The broad line width in the pXRD reflects nanocrystalline sizes as observed in the TEM imaging of selected samples available in Supporting Information Figure S4. In the data set, it is assumed that a pure phase is present if the fitting yields >95% of a single phase. For each reaction carried out, the isolated nanocarbide size is extracted from the pXRD data using Halder–Wagner pattern fitting, assuming a spherical particle. TEM analysis of Fe<sub>0.19</sub>Co<sub>0.81</sub> with 2 mmol TBAC ( $M_2$ C) and Fe<sub>0.19</sub>Co<sub>0.81</sub> with 2 mmol TBAB ( $M_2$ C) shows nanocarbides are high surface area aggregates, exhibit no detectable lattice fringes, but have a size consistent with the

Table 2. Resultant Phases for the TBAX and TBAX Concentration Studies on the 60% Fe Fe<sub>x</sub>Co<sub>y</sub>C Sample<sup>a</sup>

isolated FeCoC phase	ref card(s)	TBAX	[TBAX] (mmol)	time (h)	temp (°C)	% Fe initial	% Fe final
$M_2C$ , $M_3C$ , $M_5C_2$	ICSD:423885, ICSD:42542, ICSD:423885			1	350	60	65
$M_2C$ , $M_5C_2$	ICSD:423885, ICSD:423885	TBAF	0.5	1	350	60	58
$M_2C$ , $M_5C_2$	ICSD:423885, ICSD:423885	TBAF	1	1	350	60	57
$M_2C$ , $M_5C_2$	ICSD:423885, ICSD:423885	TBAF	2	1	350	60	58
$M_2C$ , $M_3C$	ICSD:423885, ICSD:42542	TBAC	0.1	1	350	60	60
$M_2C$ , $M_3C$ , $M_7C_3$	ICSD:423885, ICSD:42542, ICSD:76830	TBAC	0.5	1	350	60	57
$M_2C$ , $M_3C$ , $M_7C_3$	ICSD:423885, ICSD:42542, ICSD:76830	TBAC	1	1	350	60	57
$M_2C$ , $M_3C$ , $M_7C_3$	ICSD:423885, ICSD:42542, ICSD:76830	TBAC	2	1	350	60	44
$M_2C$ , $M_3C$ , $M_7C_3$	ICSD:423885, ICSD:42542, ICSD:76830	TBAC	3	1	350	60	44
$M_3C$ , $M_5C_2$	ICSD:42542, ICSD:423885	TBAB	0.5	1	350	60	55
$M_2C$ , $M_3C$ , $M_5C_2$	ICSD:423885, ICSD:42542, ICSD:423885	TBAB	1	1	350	60	46
$M_2C$ , $M_3C$ , $M_5C_2$	ICSD:423885, ICSD:42542, ICSD:423885	TBAB	2	1	350	60	21
$M_2C$ , $M_3C$ , $M_5C_2$	ICSD:423885, ICSD:42542, ICSD:423885	TBAB	3	1	350	60	6
$M_2C$ , $M_3C$ , $M_5C_2$	ICSD:423885, ICSD:42542, ICSD:423885	TBAI	0.5	1	350	60	56
$M_2C$ , $M_3C$ , $M_5C_2$	ICSD:423885, ICSD:42542, ICSD:423885	TBAI	1	1	350	60	45
$M_5C_2$ , M	ICSD:423885, ICSD:102381	TBAI	2	1	350	60	24
M	ICSD:102381	TBAI	3	1	350	60	11

<sup>&</sup>quot;Initial % Fe reflects the XRF ratio for the PBA precursor and the final % Fe reflects the XRF ratio for the carbide.

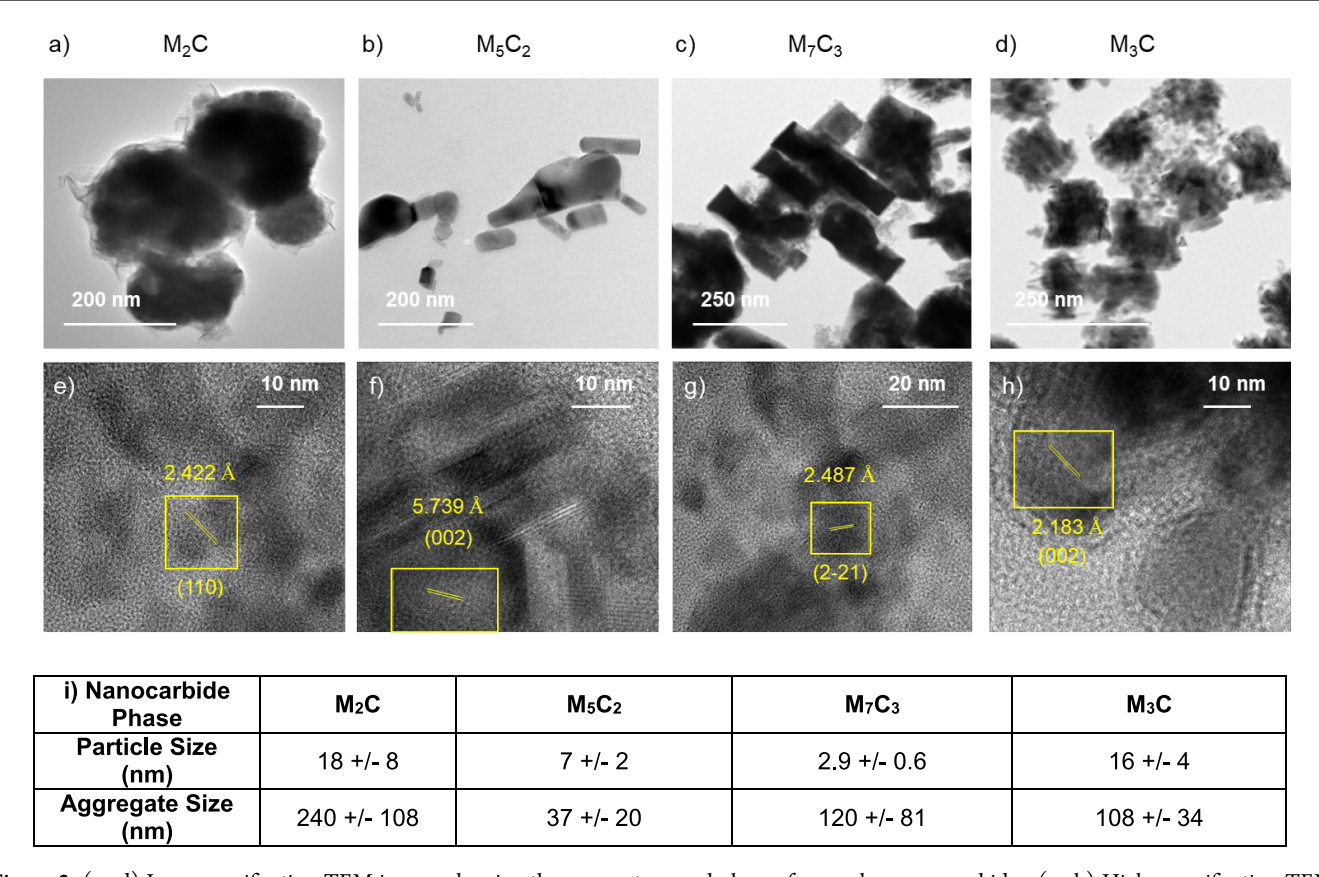


Figure 2. (a-d) Low-magnification TEM images showing the aggregate morphology of pure phase nanocarbides. (e-h) High-magnification TEM images of single particles of each carbide phase indexed to matching lattice fringes with a measured *d*-spacing. (i) Table of single particle size and aggregate size.

pXRD size analysis (TBAC: 127 nm pXRD vs TEM 142 nm; TBAB: pXRD 202 nm vs TEM 316 nm). The variation in pXRD and TEM analysis of size likely reflects the nonspherical shape, as well as grain boundaries and strain.

Inspection of the results for each reaction in Tables 1 and 2, as well as Supporting Information in Table S1, reveals that the reaction primarily produces mixed crystallographic phases. At certain combinations of TBAX and Fe:Co ratios, a single phase

can be selectively isolated for the  $M_2C$ ,  $M_7C_3$ ,  $M_5C_2$ ,  $M_3C$ , and M structural type. Representative pure phase pXRD patterns for the shown conditions are plotted in Figure 1c. The plots in Figure 1c correspond to reaction conditions for 35% Fe sample with 1 mmol of TBAB for the  $M_2C$  orthorhombic phase (COD: 1528415), 80% Fe sample with 3 mmol of TBAC to yield  $M_7C_3$  phase (ICSD: 76830), 80% Fe sample with 3 mmol of TBAI to yield the  $M_5C_2$  phase (ICSD: 423885), 60% Fe

sample with 0.1 mmol of TBAC yields the  $M_3C$  phase (ICSD: 42542), and the cubic  $Fe_xCo_{1-x}$  metal alloy (M) (ICSD: 102381) is for the 80% Fe sample with 3 mmol of TBAB. The concentration of Fe in the PBA and carbide (initial and final), as well as all other synthetic parameters used to isolate pure phase materials are reported in Tables 1, 2, and Supporting Information Table S1.

Whole pattern fitting of the pXRD supports the assignment of pure phase in the isolated nanocrystals, but due to broadening of pXRD arising from the nanoscale dimensions, the phase purity and crystallinity of the nanocrystal are difficult to fully ascertain. In Figure 2, bright field TEM images on the carbide materials are presented. Figure 2a-d shows low-magnification images (magnification 40–150kx), with Figure 2e-h showing higher magnification (800k–1.2Mx), allowing fringe analysis. Figure 2i shows the particle and aggregate size analysis from the TEM. Electron diffraction for single nanocrystals is provided in the Supporting Information (Figure S11).

TEM imaging of M<sub>5</sub>C<sub>2</sub> and M<sub>7</sub>C<sub>3</sub> shows well-defined faceted nanocrystals. It is worth noting that  $M_7C_3$  has smaller NPs (3 nm) observable at high magnification. The M<sub>2</sub>C and M<sub>3</sub>C phases exhibit aggregates of nanocrystals. The M<sub>2</sub>C sample appears to aggregate as spherical particles that have an average size of 240 nm in diameter composed of spherical particles with an average size of 18 nm (Figure 2e). The M<sub>5</sub>C<sub>2</sub> sample aggregates as truncated rectangular crystals with an average width of 37 nm, comprising smaller, somewhat rectangular particles with an average width of 7 nm (Figure 2f). The M<sub>7</sub>C<sub>3</sub> aggregates into larger more crystalline rectangular crystals with an average length of 120 nm, which are composed of smaller spherical particles with an average diameter of 3 nm (Figure 2g). The M<sub>3</sub>C sample appears to aggregate as cubes that comprise spherical particles. The aggregates have an average width of 108 nm, and the spheres have an average diameter particle size of 16 nm (Figure 2h). Interestingly, the M<sub>3</sub>C sample illustrates how the PBA's cubic sacrificial template has retained the mesoscale morphology yet is composed of smaller nanoscale carbides.

Fringe analysis of the high-magnification data confirms that the assigned phase does not exhibit polycrystallinity within a nanocrystal. The M<sub>2</sub>C phase sample was indexed based upon a d-spacing of 2.422 Å correlating M<sub>2</sub>C (110) lattice plane. Lattice fringe analysis reveals a d-spacing match of 5.739 Å to the (002) lattice plane of the M<sub>5</sub>C<sub>2</sub> phase. Lattice fringe analysis reveals a d-spacing match of 2.487 Å, which correlates to the  $(2\overline{2}1)$  lattice plane of the  $M_7C_3$  phase. The  $M_3C$ material has a d-spacing match of 2.183 Å, corresponding to the (002) lattice plane of the M<sub>3</sub>C phase. The fringe analysis assignments are confirmed by inspection of the electron diffraction patterns in Figure S11. The well-defined diffraction patterns arising from single particles are consistent with the observed faceting of the identified phases. The lack of amorphous rings or significantly different diffraction patterns supports the single-phase assumption from Figure 1.

Insight into the phase stability under the reaction conditions can be elucidated by replotting Supporting Information Table S1 in terms of a reaction phase space plot for each TBAX reaction condition (Figure 3). A cursory glance at the plot reveals reaction conditions lacking TBAX (Figure 3a), for Fe:Co ratios of <60%,  $M_3C$  is the predominate species isolated from the reaction, while at >60%  $M_5C_2$  and  $M_7C_3$  are the primary phases formed with loss of the  $M_2C$  and  $M_3C$ 

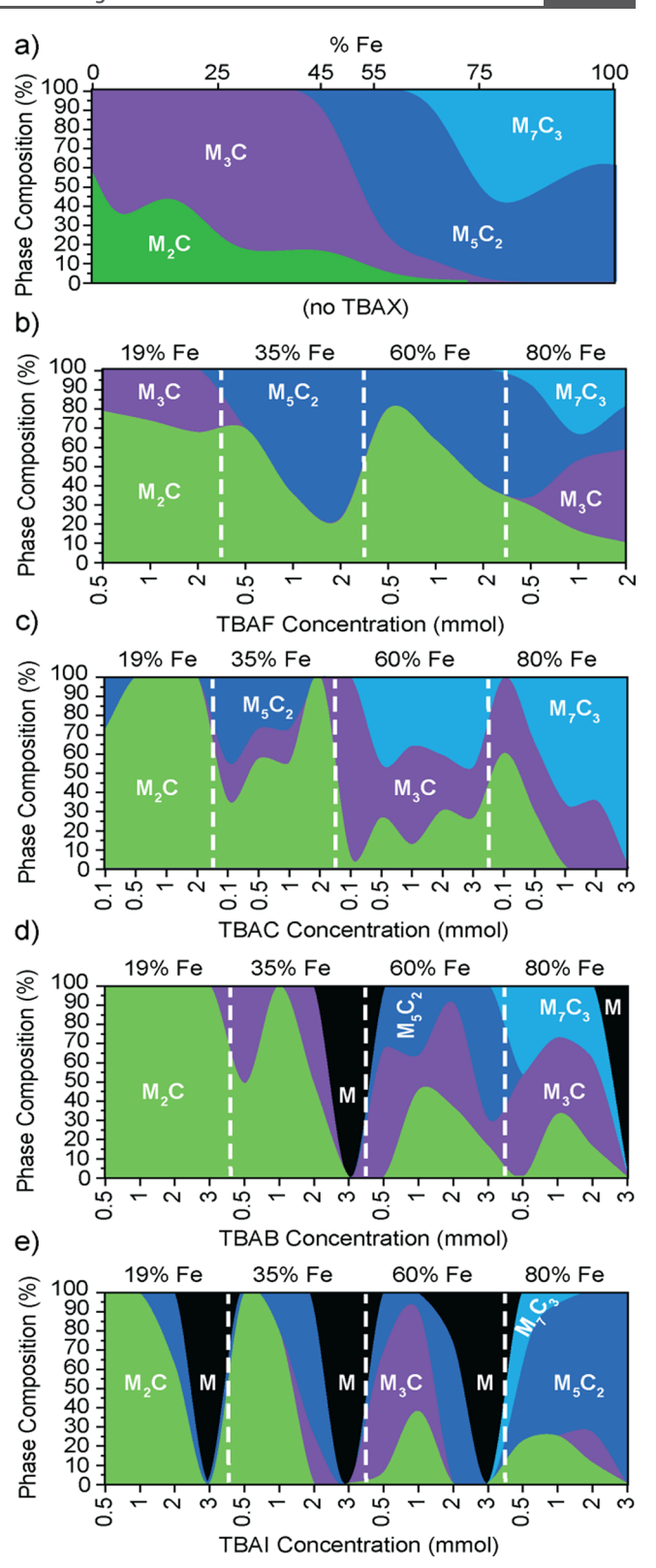


**Figure 3.** Phase diagrams produced from experimental Fe concentration, halide species, and halide concentration studies. (a) Phase composition as a function of Fe concentration without TBAX addition. (b) Phase composition as a function of TBAF and Fe concentration. (c) Phase composition as a function of TBAC and Fe concentration. (d) Phase composition as a function of TBAB and Fe concentration. (e) Phase composition as a function of TBAI and Fe concentration. Dotted white lines are placed between Fe concentration studies for the sake of clarity.

component. Addition of TBAX to the reaction leads to  $M_2C$  being the dominant component with  $M_3C$  being a minor phase for all halides and Fe:Co ratios below 60%.  $M_3C$  appears at >60% Fe:Co. At 80% Fe:Co in TBAI, the  $M_5C_2$  phase is dominant, while in TBAC  $M_7C_3$  is dominant. The results led to the conclusion that  $M_2C$ ,  $M_5C_2$ , and  $M_3C$  are competitive phases in the reaction space for the binary metal carbides. The observation of mixed carbide phases with Fe $_3C$  and Co $_2C$  being reported as the predominant observed phase for Fe:Co binaries is consistent with the observations in Figure 3. $^{2,21,28,48}$ 

Closer inspection of Figure 3 reveals that stability regions can be identified in the reaction phase space that yield pure phases as reported in Table 2. The M alloy is observed at high concentrations of TBAB and TBAI. At 3 mmol TBAF, metal fluoride contamination with metal carbides is observed, as shown in Supporting Information Figure S3. Single phase  $M_3C$  is isolated (>95% of the composition) for 60% Fe with 0.5 mmol TBAC. The pure  $M_5C_2$  phase isolated at 2 mmol TBAI for the 60% Fe sample. The pure phase  $M_7C_3$  is observed to be isolable at a high iron concentration with TBAC added. Pure phase  $M_2C$  can be isolated in TBAC and TBAB for 19% Fe at <3 mmol TBAX. The result is consistent with reports on halide directing phase iron and cobalt monometallic carbides.  $^{38,44-47}$ 

The general trends for the reaction phase space as a function of TBAX and Fe:Co metal ratio show that the halide is critical in directing the phases that form across the Fe:Co ratios. For all TBAX and TBAF reactions (Figure 3a,b), only mixed phase materials are isolated across all Fe:Co metal ratios. The phase composition varies with the Fe:Co ratio. The contribution of M<sub>2</sub>C decreases with increasing iron content under the 0 TBAX reaction condition. Increasing iron content is observed to favor moderate amounts of carbon containing carbides, while higher cobalt leads to lower carbon content phases being formed. It is noteworthy that in the TBAF reaction, the M<sub>3</sub>C phase appears in the mixed composition only at 80% iron and 19% iron, while for 0 TBAX the M<sub>3</sub>C phase shows a decreasing contribution across as iron content increases, with no appearance of the phase at 80% iron. For TBAB and TBAI (Figure 3c,d), the trend continues with a steady shift to lower carbon content in the compositions as the amount of iron increases.

Theoretical Evidence of Halide Influence on Carbide **Formation.** Metal nanocarbides can form by the diffusion of carbon into (folding in) and out of (ejection of) preformed nuclei. Earlier studies on the thermal decomposition reaction that converts PBA to the metal carbide suggest that the carbon is formed by the decomposition of the cyanide linker (CN) to form NCN- and C as products, diffusion of the NCN- out of the decomposing PBA—(nucleating metal carbide), and growth of the metal carbide by subsequent decomposition of cyanide linkers.<sup>28</sup> Growth of metal carbides from a nanometal has been shown to occur through carbon folding into the metal alloy by thermal decomposition of solvents, ligands, or other organic species in solution. <sup>23,24</sup> Thus, during carbide formation and subsequent thermal processing, it is possible that carbon diffusion represents an equilibrium problem. To understand the carbide formation at various metal contents, the stability of carbon (C) as an adatom to the surface of a metal and a carbide must be evaluated. Additionally, this equilibrium process of C diffusion is anticipated to be impacted by the binding of the halide  $(X = F^-, Cl^-, Br^-, and I^-)$  anion and, therefore, must also be taken into consideration.

In earlier reported DFT calculations on carbide formation from a metal through C diffusion into the metal, it was

observed that the binding energy (BE) of the C in the presence of chloride was impacted. <sup>49</sup> It was reported that Cl and C have competitive BEs; however, the impact of the X series on the BEs and the subsequent carbide phase was not reported. Building upon the earlier reports and to evaluate all possible C diffusion equilibrium and understand the TBAX relationship on phase isolation, first-principles DFT calculations were performed to compute the BEs of X vs C atoms on the  $Fe_3C(001)$ ,  $Co_2C(101)$ , Fe-terminated ( $FeCo)_3C(001)$ , Coterminated ( $FeCo)_3C(001)$ , and FeCo bimetallic (110) surfaces.

The first X/C/NH<sub>3</sub> binding affinity at the five available sites in each slab model is shown in Supporting Information Tables S2–S6 and as a plot in Supporting Figures S8–S10. For the Fe<sub>3</sub>C surface, the identifiable sites are the Fe top, Fe-hollow, hollow, 1-C-hollow, and 2-C-hollow (Figure S7a). For Co<sub>2</sub>C, the sites are Co top, 1-Co-hollow, hollow, C-hollow, and 2-Co-hollow (Figure S7b). The Fe terminated (FeCo)<sub>3</sub>C has sites Fe top, Co-hollow, hollow, 1-C-hollow, and 2-C-hollow (Figure S7c); while the possible sites on Co terminated (FeCo)<sub>3</sub>C are Co-top, Fe-hollow, hollow, 1-C-hollow, and 2-C-hollow (Figure S7d). On FeCo(110), the available sites are Fe-hollow, Co-hollow, Co-top, and Fe-top (Figure S7e).

Comparing the impact on C BE in the presence and absence of X provides insight into the stability of the carbide phase, indirectly reflecting the energetics of C diffusion. The BEs for the second absorption of the X, C, and the alkylamine (modeled as NH<sub>3</sub>) are shown in Figure 4g. Figure 4a–f shows the energetically most stable sites for the second adsorption of the C or X on the preadsorbed C surfaces. The reference energy of C is obtained from the energy of the C atom in the graphite bulk phase. The reference energy of the halide anions

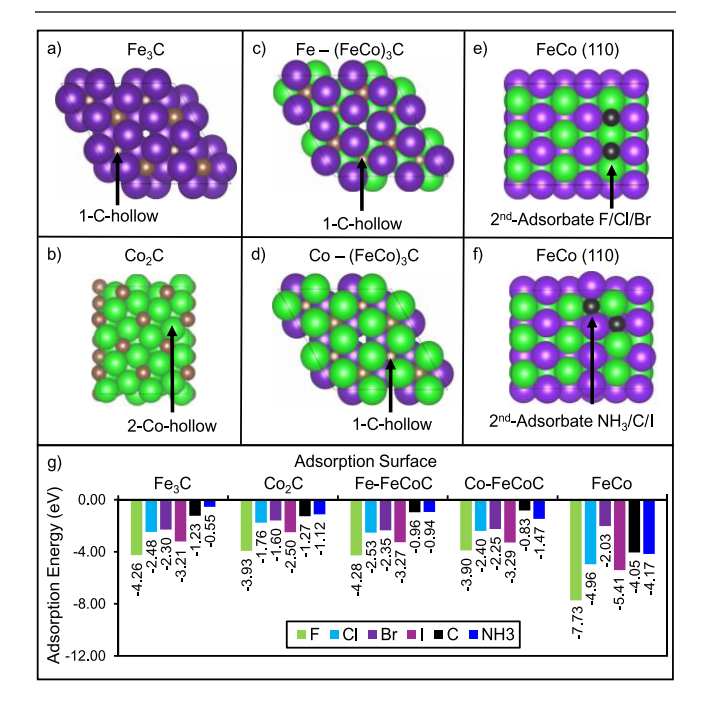


**Figure 4.** Top view of second adsorption sites on binary and ternary carbide and metal alloy surfaces. (a)  $Fe_3C(001)$  surface, (b)  $Co_2C(101)$  surface, (c) Fe-terminated FeCoC(001) surface, (d) Co-terminated FeCoC(001) surface, (e) FeCo(110) F, Cl, and Br second adsorption site, (f)  $NH_3$ , C and I second adsorption site, and (g) plot of second adsorption energies.

(X) is calculated as 1/2 the total energy of the diatomic  $X_2$  in the molecular state. The data are provided in Figure 4 and in the Supporting Information (Tables S7–S11). BE calculations using the reference energy of X obtained from X optimized in an atomic state are also performed, and the results are included in Tables S2 and S3 for the bimetallic FeCo(110) surface.

From the BE calculations, the most stable site for C adsorption on the Fe<sub>3</sub>C (001) surface is the 1-C-hollow site, with DFT calculated energies for the second adsorption (in C preadsorbed Fe<sub>3</sub>C(001) surface) of F, Cl, Br, and I as -4.26, 2.48, -2.30, and -3.21 eV respectively. The most stable site for C adsorption on the Co<sub>2</sub>C (101) surface is the 2-Cohollow, with DFT computed energies for the second adsorption of F, Cl, Br, and I as -3.93, -1.76, -1.60, and -2.50 eV. The most stable site for C binding on the Feterminated (FeCo)<sub>3</sub>C (001) surface is hollow, with DFT calculated second adsorption energy for F, Cl, Br, I of -4.28, -2.53, -2.35, and -3.27 eV. The most stable site for the Coterminated (FeCo)<sub>3</sub>C (001) surface is also the hollow with second adsorption energies for F, Cl, Br, and I of -3.90, -2.40, -2.25, and -3.29 eV. On the FeCo (110) surface, there are 2 stable sites for second F/Cl/Br and I adsorption, and these sites are at the 1-Fe-hollow and 1-Co-hollow, respectively. The DFT computed binding energies for second F, Cl, Br, I adsorption on C preadsorbed FeCo (110) surface are -7.73, -4.96, -2.03, and -5.41 eV. The opposite calculations of halide preadsorbed surfaces with a halide or carbon second adsorption are shown in SI Tables S7-S11.

Since the reactions are carried out in octadecylamine and the RNH<sub>2</sub> group is the surface passivation layer, the impact of RNH<sub>2</sub> on X/C binding at the FeCo (110) face needs to also be considered. The details of the calculations are available in Supporting Tables S2 and S7-S11. The alkylamine (RNH<sub>2</sub>) is modeled as the ammonia molecule (NH<sub>3</sub>) to mimic the passivating ligand. Our DFT results show that on the carbide phases, the BE of NH<sub>3</sub> and C are nearly identical, although the NH<sub>3</sub> is less stable on Fe<sub>3</sub>C. On the metal alloy, NH<sub>3</sub> is the second most stable, which can be rationalized by the Lewis basicity of the amine interacting with the acidic metal sites. In addition, NH<sub>3</sub> is less stable on an iron carbide phase relative to the cobalt carbide phase. This observation supports our experimental data from Figure 3 where the major phase isolated among all Fe percentages was the M<sub>2</sub>C (Co<sub>2</sub>C phase type). The observation suggests reactions carried out in alkylamines may restrict carbon diffusion into the preformed metal carbide from PBA collapse, and potentially the lowering of the barrier for carbide formation, as reported earlier.<sup>28</sup>

In the DFT models computed of preadsorbed C, the trend from greatest to least stable absorbate follows  $F^- > I^- > Br^- >$ Cl-. The order of stability reflects contributions from electronegativity and softness of X, with increased stabilization of the softest ligand (I<sup>-</sup>) due to stronger orbital overlap and for the most electronegative ligand (F<sup>-</sup>) consistent with hard-soft acid-base (HSAB) theory. This trend seen in both binary and ternary carbides is important, as it supports our experimental results of tuning carbide phase accessibility based on X species, where the energies of each X entity are different but close in magnitude. Calculations on the metal carbide and metal alloy confirm that binding the X to the surface when a C atom is preadsorbed is more favorable than adding an additional C atom. In addition, the DFT results support our earlier conclusion that RNH<sub>2</sub> passivation lowers the thermodynamic barrier for carbide formation.<sup>28</sup> This implies that the presence

of X in the metal carbide may reduce the probability of carbon diffusion into the metal carbide through C folding. The diffusion of carbon out of the material would likewise be expected to be impacted, in the presence of a bound X, as the energy of binding is higher (less negative) for C on the carbide surface, regardless of the carbide phase. By comparison, the metal alloy favors C diffusion into the alloy relative to the halides except for F. The DFT results, in general, suggest that X-mediated synthesis promotes the formation of metal-rich carbide phases, which is in agreement with experimental results in Figure 3. In Figure 3, it can be seen that the carbon content increases with decreasing halide size for a given iron/cobalt metal ratio. While the halide competes with the alkylamine for binding at the surface of the growing nanocarbide, the halide is more favorable based on DFT modeling. This suggests that the alkylamine passivating ligand is most likely not involved in phase control. Since the DFT predicts the C adsorption at the surface is nearly the same energy as the RNH2, the DFT supports the earlier conclusion that RNH<sub>2</sub> is critical for the formation of the carbide in a PBA decomposition reaction. <sup>28,50</sup>

Carbide Isolation and Stability. The experimentally observed phases and the DFT modeling predict that carbon diffusion is impacted by the presence of the halide; whether this is due to changes in metal activity, carbide formation energies, or changes in surface adsorption of C is less clear. It is well-known that TBAX thermally decomposes to generate halide ions that can form alkyl halides through SN2 reactions. 51,52 By analogy, it is believed thermal decomposition of the TBAX leads to halide release at <150 °C and subsequent halide attack on PBA lattice vacancies where water termination of metal sites exists. As a result, the formation of the nanocarbide from the PBA is anticipated to be modified by the polarizability of the halide species. To evaluate the role of the halide in the conversion to form the nanocarbide, scanning differential thermal analysis (SDT) on the 19% Fe samples at 1 mmol of TBAX is shown in Figure 5, and the temperature for

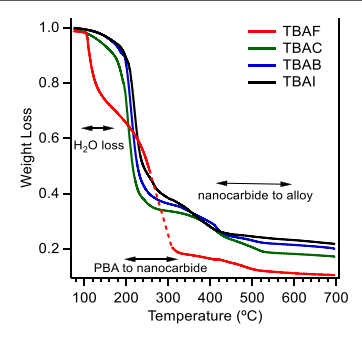


**Figure 5.** Scanning differential thermal analysis (SDT) studies on 19% Fe ( $Fe_{0.19}Co_{0.81}C$ ) with 1 mmol of TBAX added to the reaction. The water loss, PBA to nanocarbide, and nanocarbide to alloy regions are identified. The interpolated curve for TBAF is shown as a red dashed line.

carbide and alloy formation is presented in Table 3. The TBAF shows water loss at 100 °C consistent with TBAF being hygroscopic. This leads to a water loss feature at 117 °C in TBAF, but no water loss feature for TBAC, TBAB, and TBAI. In Figure 5, the TBAF SDT shows signal loss due to an instrumental error. As previously reported in the absence of TBAX, water loss from the PBA and subsequent PBA reconstruction occurs at <300 °C, the loss of NCN leads to carbide formation above 300 °C, and the alloy is isolated at

Table 3. TBAX-Dependent Temperatures for PBA to Nanocarbide and Nanocarbide to Alloy Formation

sample	PBA → carbide	$carbide \rightarrow alloy$
19% no TBAX	285 °C	570 °C
19% 1 TBAF	275 °C	505 °C
19% 1 TBAC	260 °C	510 °C
19% 1 TBAB	250 °C	515 °C
19% 1 TBAI	235 °C	510 °C

temperatures exceeding 500 °C.<sup>28</sup> In the presence of TBAX, the SDT data reveals no defined water loss event and the PBA to carbide transition occurs at lower temperature (235 °C, TBAI  $\rightarrow$  275 °C, TBAF) and the nanocarbide is thermally stable up to 505 °C, TBAF  $\rightarrow$  515 °C, TBAI. The SDT data shows that the presence of TBAX has no defined water loss event, as previously observed in the absence of TBAX, 28 which suggests replacement of the water in the PBA vacancies by the TBAX or halide ion occurs upon mixing. The transition to the alloy also shows a decrease in temperature relative to no TBAX and is largely constant across the TBAX series. Although beyond the scope of the study, the data imply that the nanocarbide is anticipated to be stable up to ~500 °C for catalytic applications, while the alloy could be used for high temperature catalysis. In SDT, the conversion to the nanocarbide shifts to a lower temperature for the halide series as a function of halide polarizability (TBAF  $\rightarrow$  TBAI). The dependence on polarizability is consistent with HSAB theory, and the DFT formation energy predictions in Figure 4. The no TBAX SDT data for the 19% sample is available in the Supporting Information (Figure S5). For the no TBAX condition, the observed SDT transitions corroborate the speculation that the presence of the TBAX halide lowers the energy barrier for carbide formation.

In Figure 6a, the accessible compositions for a given halide additive are plotted. The halide type, concentration, and ratio of Fe:Co dictate the phase that is isolated. The fact that the lowest energy carbide is  $M_5C_{2,}$  but the most isolated phase from the PBA thermal collapse is  $M_2C$ , suggests that the reaction is kinetically controlled, and the addition of halides manipulates the precursor activity to provide phase control over carbides formation. Figure 6b shows the relative energies

of the starting material (FeCo PBA), FeCo carbide, and the FeCo alloy. The results from Figure 6a lead to modification of our earlier reaction mechanism hypothesis. The model in Figure 6b now shows where the impact of halide in the barrier height for the carbide phase provides the kinetic control over the isolable carbide phase. The kinetic barrier likely reflects carbon diffusion during nucleation of the carbide phase as the PBA decomposes. In Figure 6c, the energies of the carbide phases are illustrated as compared with the precursor and alloy materials. The relative energies of the carbide phases are very close, which supports our experimental findings that specific experimental conditions (halide species, halide, and metal concentrations) are vital in the isolation of a target carbide phase.

Metal carbides exhibit a rich phase diagram, reflecting carbon migration into and out of the lattice. In addition, metal ion migration in a nanocrystal can result in phase segregation or expulsion of metals from the nanocrystal due to passivating ligand interactions. As such, the isolable metal carbide nanocrystal composition can change as a sample is held at the reaction temperature for an extended period of time. To ensure the isolated metal carbide phases are stable, the pXRD patterns for the 19, 35, 60, and 80% Fe samples were measured at 1 and 24 h for samples dissolved into octadecylamine with 2 mmol of TBAC and held at 350 °C. Inspection of Supporting Figure S4 shows no change in the pXRD pattern over the 24 h annealing experiment, indicating phase stability for the isolated samples under the reaction conditions. The annealing study confirms the isolated carbide phase from the decomposition of PBA in alkylamine is halide and metal ratio dependent, and the isolated carbide is stable under reaction conditions. The observed stability of the nanocarbide implies that carbon diffusion into and out of the material is at equilibrium.

**Electrocatalytic Activity.** It has been demonstrated that in metal carbides, the metal species and metal ratio can influence the observed overpotential for HER and OER electrocatalytic activity. The phase of the carbide has also been hypothesized to influence catalytic activity for metal carbides. In Figure 7, linear sweep voltammograms and overpotential at  $10 \text{ mA/cm}^2$  are shown for the phase pure nanocarbides presented in Figure 1 (M<sub>2</sub>C: 11% Fe, M<sub>7</sub>C<sub>3</sub>: 28% Fe, M<sub>5</sub>C<sub>2</sub>: 35% Fe, M<sub>3</sub>C: 60% Fe). The linear sweep

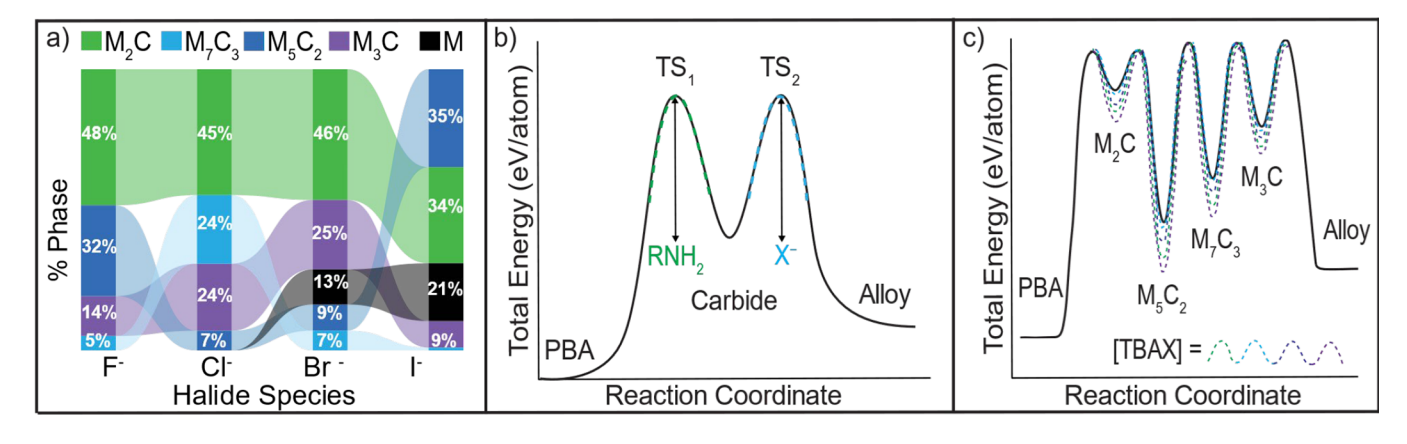


Figure 6. (a) Ribbon plot depicting carbide phase dependence on halide species. (b) Reaction coordinate diagram describing the decomposition of PBA to carbide and metal alloy. The green dotted line represents the carbide formation thermodynamic barrier that is dependent on the presence of RNH<sub>2</sub> and the light blue dotted line represents the alloy formation thermodynamic barrier which is dependent on the presence of  $X^-$ . (c)The relative energies for each unique carbide phase. The colored dotted lines represent modulation of the thermodynamic barrier by varying the halide species (TBAX) and halide concentrations ([TBAX]).

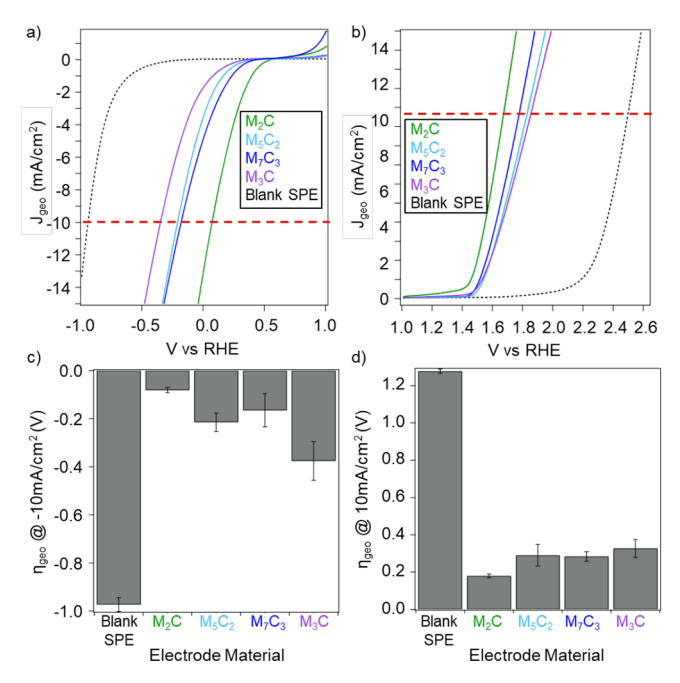


Figure 7. Linear sweep voltammograms to evaluate electrocatalytic performance in HER (a) and the OER (b) for each pure phase FeCo nanocarbide. The red dotted line represents the standard current densities required to be considered a catalyst. (c,d) Bar charts comparing the HER and OER overpotentials for each sample. Purple represents  $M_2C_1$ , dark blue represents  $M_7C_2$ , light blue represents  $M_5C_2$ , green represents  $M_2C_1$ , and black represents the blank electrode.

voltammograms were measured under alkaline conditions for the OER and acidic conditions for the HER on samples drop cast from methanol onto a carbon screen printed electrode. The lowest observed overpotential for OER and HER is for the  $M_2C$  phase, with an increase in overpotential occurring as total metal content in the carbide increases. Inspection of the OER and HER overpotentials for the carbide phase studies in Table 4 reveals that the  $M_2C$  and  $M_7C_3$  materials would be

Table 4. Phase-Dependent HER, OER, and Combined Overpotential Were Measured by Linear Sweep Voltammetry

phase	% Fe	$\eta_{ m HER}$ (V)	$\eta_{\mathrm{OER}} \left( \mathrm{V} \right)$	$\Delta\eta$ (V) $\eta_{ m OER}-\eta_{ m HER}$
$M_2C$	11	-0.082	0.180	0.262
$M_7C_3$	28	-0.165	0.284	0.449
$M_5C_2$	35	-0.215	0.290	0.505
$M_3C$	60	-0.376	0.327	0.703

appropriate for application as an effective electrocatalyst for solar water splitting, <sup>56</sup> since the combined overpotentials is less than 0.45 V. Further studies to interrogate the potential of nanocarbides for solar water splitting are underway.

We have reported that increasing iron content leads to a lower decrease in overpotential for <20% iron and an increase in overpotential at higher iron percentages in mixed phase Fe/Co carbides.<sup>21</sup> For the reported data, it is important to note that in addition to changes in metal to carbon content in the phase, the Fe to Co ratio is changing with a higher Fe ratio corresponding to a higher metal content in the nanocarbide. The observation of a lower overpotential for lower metal content carbides in Figure 7 explains the observation in the

previous article, implying phase purity is important in lowering overpotential in addition to metal concentration. The data clearly indicates that to fully evaluate electrocatalytic activities both phase and metal ratio must be evaluated simultaneously.

# CONCLUSIONS

It is known that in thermal collapse mechanisms, ligand additives can control not only the rate of reaction but also the phase of the isolated material.<sup>57</sup> In the case of PBA decomposition of bimetallic PBA mesocrystal precursors, the addition of halides is vital to the systematic control of metal carbide. The developed synthetic approach provides a means to selectively isolate targeted, single phase ternary  $(Fe_xCo_{1-x})_yC_z$  materials by judicious choice of the halide additive and its concentration to control carbon adsorption and carbide growth. The study supports the hypothesis that halides facilitate the isolation of a targeted carbide in the thermal decomposition reaction following the initial PBA to carbide step. The role of halides in controlling growth appears to be reflective of the carbon diffusion equilibrium inside and out of the isolated carbide. Theoretical modeling supports the experimental conclusion that addition of halides to a PBA thermal decomposition reaction impacts the growth behavior and carbon incorporation into the isolable nanocarbides. The observed experimental dependence of the halide on the carbide phase, coupled to DFT modeling supports a mechanism wherein cocoordination of RNH<sub>2</sub> and the halide impacts the thermodynamic stability of the carbon. The DFT observations support a two-step mechanism where carbon rich carbides form as PBA collapses, followed by carbon diffusion out of the material, leading to metal rich phases. From the DFT BEs, the lower carbon stability in the Fe-terminated carbide would suggest that a higher metal to carbon material would be stabilized with increasing iron content. The effect on the carbide phase with increasing iron was reported for mixed phase Fe-Co carbides previously.<sup>21</sup> The isolated nanocarbides are thermally stable under the reaction conditions and over a wide temperature range after isolation as shown by SDT measurements. The DFT modeling supports that the control reflects regulating the flow of carbon in and out of the materials.

Our experimental results coupled with theory provide a guide to enable future researchers to make pure phase ternary carbides for catalytic studies, and potential for formation of phase control to the broader MX-ide family (O, P, N, S, Se, and Te) which have been heavily studied in OER and HER electrocatalytic reactions.  $^{15,17,62-70,21,48,53,54,58-61}$  The phase pure carbides exhibit electrocatalytic activity that is phase dependent and could be used in solar catalysis based on the HER/OER overpotentials. Regardless of the future applications, the coupling of theoretical modeling in the prediction of reaction outcome is a power tool that enables a rapid advancement of materials. Further studies are underway investigating the catalytic and magnetic properties of the ternary  $(Fe_xCo_{1-x})_yC_z$  range. As well as expanding this work to related materials.

# **■** EXPERIMENTAL SECTION

ı

**Materials.** All commercially available reagents were used without further purification. Precursors for FeCo PBAs are  $K_3Co(CN)_6$  and  $K_3Fe(CN)_6$  (Sigma-Aldrich, >99%), KCl (Sigma-Aldrich, 98%), CoCl<sub>2</sub>·6H<sub>2</sub>O (Thermo Fisher, >99%), and FeCl<sub>2</sub>·4H<sub>2</sub>O (Thermo Fischer, >99%). Solvents used for synthesis were ultrapure water

(18.2  $\Omega$ /cm, Thermo Fisher Barnstead E-Pure Ultrapure filtration system), octadecylamine (Acros Organics, 90%), acetone (VWR, ACS grade), and toluene (VWR, ACS grade).

Synthesis of FeCo PBA Precursors. To produce the PBA precursors, two solutions are prepared and combined, creating a coordination polymer through a precipitation reaction. The stoichiometric ratios of the metals are controlled by adjusting the ratio of precursors in these solutions. In solution one, 5 mmol of KCl, x mmol  $K_3Fe(CN)_6$  (x = 0, 0.1, 0.5, 0.9, 1), 1 - x mmol  $K_3Co(CN)_6$ (y = 1, 0.9, 0.5, 0.1, 0), 10 mL of ultrapure water, and a magnetic stir bar are added to a 100 mL round-bottom flask. Solution two consists of 1 mmol of either FeCl<sub>2</sub> (>50% Fe) or CoCl<sub>2</sub> (<50% Fe) and 20 mL of ultrapure water are added to a 50 mL beaker. Solution two is then dropwise added to solution one at a rate of 5 mL/min and vigorously stirred. The subsequent reaction solution is left on the stirring for 1 h to grow the PBA. The PBA are collected via centrifugation, washed with 30 mL of ultrapure water and dried in a furnace at 90 °C for approximately 1.5 h, or until dry. The PBA precursors are characterized using pXRD, SEM, and XRF.

**Synthesis of FeCo Nanocarbide** ( $Fe_xCo_{1-x})_yC_z$ . In the typical synthesis, 200 mg of solid PBA, 0.1–3 mmol of tetrabutylammonium halide (TBAX, where  $X = F^-$ ,  $Cl^-$ ,  $Br^-$ ,  $I^-$ ), and 20 mL of octadecylamine (ODA) are added to a three-neck round-bottom flask equipped with a condenser and heated to 330 °C under inert air for 1 h. The reaction is subsequently quenched using toluene, and the resultant nanocarbide is collected via centrifugation. The nanoparticles are washed with toluene (3×), acetone (1×), ultrapure water (3×), and acetone (1×). The nanoparticles are dried in an oven at 90 °C for 15 min. The nanoparticles are characterized using pXRD and XRF.

Material Characterization. pXRD patterns of PBAs and PBA derived carbides were collected at room temperature on a Rigaku Miniflex powder diffractometer (Cu  $K\alpha$  source,  $\lambda=1.54$  Å, Supporting Figure S3). The contributions of various crystalline phases were fitted and calculated as a percentage for each Fe<sub>x</sub>Co<sub>1-x</sub>C<sub>y</sub> using the Halder–Wagner method as shown in Supporting Figure S4. The elemental ratios in both PBA and nanocarbide were confirmed using XRF on a Panalytical Epsilon XRF analyzer (Cu  $K\alpha$  source, Supporting Figure S2). Size and morphology of PBA precursors were investigated via SEM imaging (FEI Nova 400, 15 keV, Supporting Figure S1). Size and morphology of the nanocarbides were estimated using ImageJ software (sample size = 10 particles) via TEM images, collected on a Tecnai Osiris TEM operating at 200 kV (Figure 2).

Computational Methods. We used spin-polarized DFT 71 calculations within the Vienna Ab initio Simulation Package (VASP). The generalized gradient approximation (GGA)<sup>74</sup> was used to account for the exchange correlations effect proposed by Perdew-Burke-Ernzerhof (PBE), and electron-ion interactions were described by the projected augmented plane wave (PAW)<sup>75</sup> potentials. Bulk Fe in body-centered cubic (bcc) models the monometallic (101) surface, and FeCo in the bcc structure is taken to model the bimetallic (110) surface. Both surfaces consist of 72 atoms in an A-B-A-B stacking pattern; the monometallic surface has 72 Fe atoms, and the bimetallic surface consists of 36 Fe and Co atoms. The monometallic carbides observed in our experiment in hexagonal Fe<sub>3</sub>C and orthorhombic Co<sub>2</sub>C are used to model the Fe<sub>3</sub>C(001) and Co<sub>2</sub>C(101) surfaces, respectively; Fe<sub>3</sub>C(001) surface consist of 48 Fe and 16 C atoms, while Co<sub>2</sub>C(101) surface consists of 40 Co and 20 C atoms. The bimetallic carbide (FeCo)<sub>3</sub>C(001) surface was constructed by replacing three Fe atoms with Co atoms in a hexagonal Fe<sub>3</sub>C structure. It can have Fe- and Co-terminated surfaces; both terminated surfaces have 24 Co, Fe, and 16 C atoms. We used a supercell approach with a 3 × 3-unit cell (metallic and bimetallic surface) and 2 × 2-unit cell (monometallic barbide and bimetallic carbide) having four layers in a slab; the bottom two layers were fixed at the bulk position, and the top two layers were allowed to relax. Periodic interaction between the slabs was minimized by a vacuum of 18 Å along the c-axis. We set an energy cutoff of 420 eV for total energy calculations, and a Brillouin zone sampling was carried out using a Monkhorst–Pack<sup>75</sup> grid of  $3 \times 3 \times 1$  for the surface slab.

A relaxed geometry was obtained when the force on each atom was less than 0.01 eV/Å and the energy convergence was  $10^{-5}$  eV.

**Electrode Preparation.** A catalyst slurry was prepared using 1 mg of catalyst powder and 1 mL of methanol. The slurry was sonicated until homogenized  $\sim$ 1 min, and then the suspension was dropcasted onto the carbon working electrode (5 mm  $\times$  4 mm) of a Pine Instruments carbon screen printed electrode (SPE). The mass loading onto the surface of the electrode is approximately 0.1 mg/cm<sup>2</sup>. The electrodes were dried at room temperature for about 30 min before electrochemical measurements were performed.

**Electrochemical Measurements.** All electrochemical measurements were performed using a Pine Research 3 electrode screen printed electrode system connected to a CH 660E potentiostat. The SPEs contain a carbon working and counter electrodes as well as a Ag/AgCl reference electrode. For OER measurements, 1 M KOH electrolyte was used, and for HER, 1 M  $\rm H_2SO_4$  electrolyte was used. All potentials were converted to the reversible hydrogen electrode potential using eq 1.

$$E_{\text{vs.RHE}} = E_{\text{vs.Ag/AgCl}} + 1.009 \text{ V} \tag{1}$$

The potentials versus RHE were then used to calculate the overpotentials for the OER using eq 2.

$$\eta = E_{\text{vs.RHE}} - 1.23 \text{ V} \tag{2}$$

# ASSOCIATED CONTENT

# Supporting Information

The Supporting Information is available free of charge at https://pubs.acs.org/doi/10.1021/acs.chemmater.4c00701.

Material characterization of PBA precurors, Halder–Wagner fitting of pXRD patterns for as-synthesized nanocarbides, reference tables of synthetic protocol and resultant nanocarbide phases, and reference tables of calculated DFT adsorption energies (PDF)

# AUTHOR INFORMATION

# **Corresponding Authors**

Shyam Kattel — Department of Physics, Florida A&M University, Tallahassee, Florida 32310, United States; orcid.org/0000-0002-5843-5889; Email: shyam.kateel@famu.edu

Geoffrey Strouse — Department of Chemistry and Biochemistry, Florida State University, Tallahassee, Florida 32306, United States; orcid.org/0000-0003-0841-282X; Email: strouse@chem.fsu.edu

# **Authors**

Isabella Bertini — Department of Chemistry and Biochemistry, Florida State University, Tallahassee, Florida 32306, United States; oocid.org/0000-0001-8365-7259

Bipin Lamichhane — Department of Physics, Florida A&M University, Tallahassee, Florida 32310, United States;
orcid.org/0000-0002-9503-083X

Samantha Bell – Department of Chemistry and Biochemistry, Florida State University, Tallahassee, Florida 32306, United States

**Keyou Mao** – Department of Industrial and Manufacturing Engineering, FAMU-FSU College of Engineering, Tallahassee, Florida 32310, United States

Complete contact information is available at: https://pubs.acs.org/10.1021/acs.chemmater.4c00701

#### **Author Contributions**

Precursor and PBA decomposition were performed by I.B. and S.B. Material characterizations were executed by I.B. All DFT calculations and associated content were prepared by B.L. assisted by S.K. The manuscript was prepared by I.B. and G.F.S. The manuscript was edited by I.B., G.F.S., B.L., and S.K.

#### Notes

The authors declare no competing financial interest.

# ACKNOWLEDGMENTS

G.F.S. wishes to thank the National Science Foundation (NSF) (CHE-1608364) "SusChEM: Understanding Microwave Interactions to Control Magnetic Nanocrystal Growth from a Single Source Precursor" and NSF (DMR-1905757) "Tuning Plasmonic and Magneto-Plasmonic Behavior in 4-d Transition Metal Doped Indium Oxide" for funding. This project used instrumentation provided by the X-ray Crystallography Center (FSU075000X-RAY) and the Materials Characterization Laboratory (FSU075000MAC) at the FSU Department of Chemistry and Biochemistry. Additionally, G.F.S. would like to thank Dr. Raaj Winfred for collecting a portion of the thermal data. S.K. acknowledges the finding from National Science Foundation: Excellence in Research Award (EIR CBET-2200456). This work used computational resources at the San Diego Supercomputer Center (SDSC) through allocation CHE200036 from the Advanced Cyberinfrastructure Coordination Ecosystem: Services & Support (ACCESS) program, which is supported by National Science Foundation grants #2138259, #2138286, #2138307, #2137603, and #2138296. This research used the Theory and Computation facility of the Center for Functional Nanomaterials (CFN), which is a U.S. Department of Energy Office of Science User Facility, at Brookhaven National Laboratory under Contract No. DE-SC0012704.

# ABBREVIATIONS

TBAF, tetrabutylammonium fluoride; TBAC, tetrabutylammonium chloride; TBAB, tetrabutylammonium bromide; TBAI, tetrabutylammonium iodide; TBAX, tetrabutylammonium halides;  $(Fe_xCo_{1-x})_yC_z$ , iron cobalt carbide with various ratios of iron and cobalt

# REFERENCES

- (1) Davydov, S. V. Phase Equilibria in the Carbide Region of Iron—Carbon Phase Diagram. *Steel Transl.* **2020**, *50*, 888–896.
- (2) Nguyen, E. T.; McBride, J. R.; Mao, K.; Martin, P. A.; Strouse, G. F. Metal Carbide Nanocrystal Nucleation and Growth in a Transition Metal Coordination Polymer. *J. Phys. Chem. C* **2022**, *126*, 20636–20643.
- (3) Raghavan, V. C-Co-Fe (Carbon-Cobalt-Iron). J. Phase Equilibria Diffus. 2009, 30, 378.
- (4) Cheng, J.; Hu, P.; Ellis, P.; French, S.; Kelly, G.; Lok, C. M. Density Functional Theory Study of Iron and Cobalt Carbides for Fischer—Tropsch Synthesis. *J. Phys. Chem. C* **2010**, *114*, 1085–1093.
- (5) Wezendonk, T. A.; Sun, X.; Dugulan, A. I.; van Hoof, A. J. F.; Hensen, E. J. M.; Kapteijn, F.; Gascon, J. Controlled Formation of Iron Carbides and Their Performance in Fischer—Tropsch Synthesis. *J. Catal.* **2018**, *362*, 106–117.
- (6) Li, S. Iron Carbides: Control Synthesis and Catalytic Applications in COx Hydrogenation and Electrochemical HER. *Adv. Mater.* **2019**, *31*, No. 1901796.
- (7) Yang, C.; et al. Construction of Synergistic Fe5C2/Co Heterostructured Nanoparticles as an Enhanced Low Temperature Fischer—Tropsch Synthesis Catalyst. *ACS Catal.* **2017**, *7*, 5661–5667.

- (8) Chang, Q.; et al. Relationship between Iron Carbide Phases ( $\epsilon$ -Fe2C, Fe7C3, and  $\chi$ -Fe5C2) and Catalytic Performances of Fe/SiO2 Fischer—Tropsch Catalyst. *ACS Catal.* **2018**, 8 (4), 3304–3316.
- (9) De Smit, E.; Cinquini, F.; Beale, A. M.; Safonova, O. V.; Van Beek, W.; Sautet, P.; Weckhuysen, B. M. Stability and Reactivity of  $\varepsilon$ -X- $\theta$  Iron Carbide Catalyst Phases in Fischer—Tropsch Synthesis: Controlling Mc. *J. Am. Chem. Soc.* **2010**, *132*, 14928—14941.
- (10) Liu, Q. Y.; Shang, C.; Liu, Z. P. In Situ Active Site for Fe-Catalyzed Fischer—Tropsch Synthesis: Recent Progress and Future Challenges. J. Phys. Chem. Lett. 2022, 13, 3342—3352.
- (11) Louw, J. D.; Van Den Berg, J. P.; Ferreira, L. C.; Pienaar, J. J. Appearance of FeC in a Hydrocarbon Synthesis Catalyst. *J. Am. Chem. Soc.* 1957, 79, 5899–5902.
- (12) Liu, X. W.; et al. Iron Carbides in Fischer—Tropsch Synthesis: Theoretical and Experimental Understanding in Epsilon-Iron Carbide Phase Assignment. *J. Phys. Chem. C* **2017**, *121*, 21390–21396.
- (13) Mendoza-Garcia, A.; Su, D.; Sun, S. Sea Urchin-like Cobalt-Iron Phosphide as an Active Catalyst for Oxygen Evolution Reaction. *Nanoscale* **2016**, *8*, 3244–3247.
- (14) Wang, H.; Zhu, S.; Deng, J.; Zhang, W.; Feng, Y.; Ma, J. Transition Metal Carbides in Electrocatalytic Oxygen Evolution Reaction. *Chin. Chem. Lett.* **2021**, *32*, 291–298.
- (15) Feng, C.; Bilal Faheem, M.; Fu, J.; Xiao, Y.; Li, C.; Li, Y.; Faheem, M. B.; Fu, J.; Xiao, Y.; Li, C.; Li, Y. Fe-Based Electrocatalysts for Oxygen Evolution Reaction: Progress and Perspectives. *ACS Catal.* **2020**, *10*, 4019–4047.
- (16) Mu, A.; Scheu, C.; Pokharel, A.; Bo, S.; Bein, T.; Fattakhovarohlfing, D. Iron-Doped Nickel Oxide Nanocrystals Alkaline Water Splitting. *ACS Nano* **2015**, *9*, 5180–5188.
- (17) Zhang, G.; Yuan, J.; Liu, Y.; Lu, W.; Fu, N.; Li, W.; Huang, H. Boosting the Oxygen Evolution Reaction in Non-Precious Catalysts by Structural and Electronic Engineering. *J. Mater. Chem. A* **2018**, *6*, 10253–10263.
- (18) Dutta, A.; Pradhan, N. Developments of Metal Phosphides as Efficient OER Precatalysts. *J. Phys. Chem. Lett.* **2017**, *8*, 144–152.
- (19) Chuang, C. H.; Hsiao, L. Y.; Yeh, M. H.; Wang, Y. C.; Chang, S. C.; Tsai, L. D.; Ho, K. C. Prussian Blue Analogue-Derived Metal Oxides as Electrocatalysts for Oxygen Evolution Reaction: Tailoring the Molar Ratio of Cobalt to Iron. *ACS Appl. Energy Mater.* **2020**, 3, 11752–11762.
- (20) Huang, J.; Xu, P.; Gao, T.; Huangfu, J.; Wang, X. jie; Liu, S.; Zhang, Y.; Song, B. Controlled Synthesis of Hollow Bimetallic Prussian Blue Analog for Conversion into Efficient Oxygen Evolution Electrocatalyst. ACS Sustain. Chem. Eng. 2020, 8 (2), 1319–1328.
- (21) Ritz, A. J.; Bertini, I. A.; Nguyen, E. T.; Strouse, G. F.; Lazenby, R. A. Electrocatalytic Activity and Surface Oxide Reconstruction of Bimetallic Iron-Cobalt Nanocarbide Electrocatalysts for the Oxygen Evolution Reaction. *RSC Advances.* **2023**, *13*, 33413–33423.
- (22) Wang, J.; Hou, Y. Iron Carbide Nanostructures: An Emerging Material for Tumor Theranostics. *Accounts Mater. Res.* **2022**, *3*, 89–90
- (23) Wang, X.; Zhu, K.; Ju, Y.; Li, Y.; Li, W.; Xu, J.; Hou, Y. Iron Carbides: Magic Materials with Magnetic and Catalytic Properties. *J. Magn. Magn. Mater.* **2019**, *489*, No. 165432.
- (24) Ye, Z.; Zhang, P.; Lei, X.; Wang, X.; Zhao, N.; Yang, H. Iron Carbides and Nitrides: Ancient Materials with Novel Prospects. *Chem.—A Eur. J.* **2018**, *24*, 8922–8940.
- (25) Naraghi, R.; Selleby, M.; Ågren, J. Thermodynamics of Stable and Metastable Structures in Fe-C System. *Calphad Comput. Coupling Phase Diagrams Thermochem.* **2014**, *46*, 148–158.
- (26) Dey, G. R.; Soliman, S. S.; McCormick, C. R.; Wood, C. H.; Katzbaer, R. R.; Schaak, R. E. Colloidal Nanoparticles of High Entropy Materials: Capabilities, Challenges, and Opportunities in Synthesis and Characterization. *ACS Nanosci. Au* **2024**, *4*, 3–20.
- (27) Soliman, S. S.; Dey, G. R.; Mccormick, C. R.; Schaak, R. E. Temporal Evolution of Morphology, Composition, and Structure in the Formation of Colloidal High-Entropy Intermetallic Nanoparticles. *ACS Nano* **2023**, *17*, 16147–16159.

- (28) Hardy, D. A.; Nguyen, E. T.; Parrish, S. E.; Schriber, E. A.; Schlicker, L.; Gili, A.; Kamutzki, F.; Hohman, J. N.; Strouse, G. F. Prussian Blue Iron—Cobalt Mesocrystals as a Template for the Growth of Fe/Co Carbide (Cementite) and Fe/Co Nanocrystals. *Chem. mater.* **2019**, *31* (19), 8163—8173.
- (29) Bhadeshia, H. K. D. H.; Chintha, A. R.; Lenka, S. Critical Assessment 34: Are  $\chi$  (Hägg),  $\eta$  and  $\epsilon$  Carbides Transition-Phases Relative to Cementite in Steels? *Mater. Sci. Technol.* **2019**, 35, 1301–1305.
- (30) Okamoto, H. The C-Fe (Carbon-Iron) System. *J. Phase Equilib.* **1992**, *13*, 543–565.
- (31) Ishlda, K.; Nishlzawa, T. Phase Diagram Evaluations: Section II The C-Co (Carbon-Cobalt) System Equilibrium Diagram. *J. Phase Equilib.* **1991**, *12*, 417–424.
- (32) Tang, T.; Duan, Z.; Baimanov, D.; Bai, X.; Liu, X.; Wang, L.; Wang, Z.; Guan, J. Synergy between Isolated Fe and Co Sites Accelerates Oxygen Evolution. *Nano Res.* **2023**, *16*, 2218–2223.
- (33) Ali Ehsan, M.; Saeed Hakeem, A.; Rehman, A. Synergistic Effects in Bimetallic Pd-CoO Electrocatalytic Thin Films for Oxygen Evolution Reaction. *Sci. Rep.* **2020**, *10*, No. 14469.
- (34) Jiang, J.; Zhou, X. L.; Lv, H. G.; Yu, H. Q.; Yu, Y. Bimetallic-Based Electrocatalysts for Oxygen Evolution Reaction. *Adv. Funct. Mater.* **2023**, 33, No. 2212160.
- (35) Bai, L.; Hsu, C. S.; Alexander, D. T. L.; Chen, H. M.; Hu, X. A Cobalt-Iron Double-Atom Catalyst for the Oxygen Evolution Reaction. *J. Am. Chem. Soc.* **2019**, *141*, 14190–14199.
- (36) Li, K.; Li, Y.; Peng, W.; Zhang, G.; Zhang, F.; Fan, X. Bimetallic Iron-Cobalt Catalysts and Their Applications in Energy-Related Electrochemical Reactions. *Catalysts.* **2019**, *9*, 762.
- (37) Nikitenko, S. I. Synthesis of Highly Magnetic, Air-Stable Iron ± Iron Carbide Nanocrystalline Particles by Using Power Ultrasound. *Halterman Compr. Asymmetric Catal.* **2001**, *113*, 206–215.
- (38) El-Gendy, A. A.; Bertino, M.; Clifford, D.; Qian, M.; Khanna, S. N.; Carpenter, E. E. Experimental Evidence for the Formation of CoFe2C Phase with Colossal Magnetocrystalline-Anisotropy. *Appl. Phys. Lett.* **2015**, *106*, 213109.
- (39) Neeli, S. T.; Ramsurn, H.; Ng, C. Y.; Wang, Y.; Lu, J. Removal of Cr (VI), As (V), Cu (II), and Pb (II) Using Cellulose Biochar Supported Iron Nanoparticles: A Kinetic and Mechanistic Study. *J. Environ. Chem. Eng.* **2020**, *8*, 103886.
- (40) Yuan, X.; Zhou, Y.; Huo, C.; Guo, W.; Yang, Y.; Li, Y.; Wen, X. Crystal Structure Prediction Approach to Explore the Iron Carbide Phases: Novel Crystal Structures and Unexpected Magnetic Properties. J. Phys. Chem. C 2020, 124, 17244–17254.
- (41) Li, S. J.; Ishihara, M.; Yumoto, H.; Aizawa, T.; Shimotomai, M. Characterization of Cementite Films Prepared by Electron-Shower-Assisted PVD Method. *Thin Solid Films* **1998**, *316*, 100–104.
- (42) Dong, X. L.; et al. Characterization of Ultrafine  $\gamma$ -Fe(C),  $\alpha$ -Fe(C) and Fe3C Particles Synthesized by Arc-Discharge in Methane. *J. Mater. Sci.* **1998**, 33, 1915–1919.
- (43) Starchikov, S. S.; et al. Evolution of the Phase Composition, Crystal Structure and Magnetic Properties of Core@shell Nanoparticles Obtained during Conversion of Ferrocene at High Pressure and High Temperature. *Appl. Surf. Sci.* 2023, 615, 156269.
- (44) Yang, C.; Zhao, H.; Hou, Y.; Ma, D. Fe5C2 Nanoparticles: A Facile Bromide-Induced Synthesis and as an Active Phase for Fischer—Tropsch Synthesis. *J. Am. Chem. Soc.* **2012**, *134*, 15814—15821.
- (45) Li, S.; et al. Wet-Chemistry Synthesis of Cobalt Carbide Nanoparticles as Highly Active and Stable Electrocatalyst for Hydrogen Evolution Reaction. *Nano Res.* **2017**, *10*, 1322–1328.
- (46) Williams, B.; Clifford, D.; El-Gendy, A. A.; Carpenter, E. E. Solvothermal Synthesis of Fe7C3 and Fe3C Nanostructures with Phase and Morphology Control. *J. Appl. Phys.* **2016**, *120*, 33904.
- (47) Huba, Z. J.; Carpenter, E. E. Size and Phase Control of Cobalt-Carbide Nanoparticles Using OH- and Cl- Anions in a Polyol Process. *J. Appl. Phys.* **2012**, *111*, 7–529.

- (48) Nguyen, E. T. A Single Source, Scalable Route for Direct Isolation of Earth-Abundant Nanometal Carbide Water-Splitting Electrocatalysts. *Inorg. Chem.* **2024**, *2022*, 61.
- (49) Yang, Z.; Zhao, T.; Huang, X.; Chu, X.; Tang, T.; Ju, Y.; Wang, Q.; Hou, Y.; Gao, S. Modulating the Phases of Iron Carbide Nanoparticles: From a Perspective of Interfering with the Carbon Penetration of Fe@Fe3O4 by Selectively Adsorbed Halide Ions. *Chem. Sci.* 2017, 8, 473–481.
- (50) Nguyen, E. T.; Mcbride, J. R.; Mao, K.; Martin, P. A.; Strouse, G. F. Metal Carbide Nanocrystal Nucleation and Growth in a Transition Metal Coordination Polymer. *J. Phys. Chem. C* **2022**, *126* (48), 20636–20643.
- (51) Sun, H.; Dimagno, S. G. Anhydrous Tetrabutylammonium Fluoride. J. Am. Chem. Soc. 2005, 127, 2050–2051.
- (52) Charette, A. B.; Chinchilla, R.; Nájera, C. Tetrabutylammonium Bromide. *Encycl. Reagents Org. Synth.* **2007**.
- (53) Li, Z.; Zhao, T.-T.; Jiang, W.-J.; Niu, S.; Wu, M.; Hu, J.-S. Bimetal Prussian Blue as a Continuously Variable Platform for Investigating the Composition—Activity Relationship of Phosphides-Based Electrocatalysts for Water Oxidation. ACS Appl. Mater. & Interfaces 2018, 10, 35904—35910.
- (54) Wu, Z.-P. Non-Noble-Metal-Based Electrocatalysts toward the Oxygen Evolution Reaction. *Adv. Funct. Mater.* **2020**, *30*, No. 1910274.
- (55) Zhang, L.; Ren, X.; Guo, X.; Liu, Z.; Asiri, A. M.; Li, B.; Chen, L.; Sun, X. Efficient Hydrogen Evolution Electrocatalysis at Alkaline PH by Interface Engineering of Ni2P-CeO2. *Inorg. Chem.* **2018**, *57*, 548–552.
- (56) McCrory, C.; Jung, S.; C. Peters, J.; F. Jaramillo, T. Benchmarking Heterogeneous Electrocatalysts for the Oxygen Evolution Reaction. *J. Am. Chem. Soc.* **2013**, *135*, 16977–16987.
- (57) Ghosh, S.; Manna, L. The Many "Facets" of Halide Ions in the Chemistry of Colloidal Inorganic Nanocrystals. *Chem. Rev.* **2018**, *118*, 7804–7864.
- (58) Sun, H.; Zhu, Y.; Jung, W. Tuning Reconstruction Level of Precatalysts to Design Advanced Oxygen Evolution Electrocatalysts. *Molecules* **2021**, 26, 5476.
- (59) Saad, A. Ordered Mesoporous Cobalt—Nickel Nitride Prepared by Nanocasting for Oxygen Evolution Reaction Electrocatalysis. *Adv. Mater. Interfaces* **2019**, *6*, No. 1900960.
- (60) Ding, X.; et al. An Fe Stabilized Metallic Phase of NiS2 for the Highly Efficient Oxygen Evolution Reaction. *Nanoscale* **2019**, *11*, 23217–23225.
- (61) Danilovic, N.; et al. Activity—Stability Trends for the Oxygen Evolution Reaction on Monometallic Oxides in Acidic Environments. *J. Phys. Chem. Lett.* **2014**, *5*, 2474—2478.
- (62) Fan, K.; et al. Direct Observation of Structural Evolution of Metal Chalcogenide in Electrocatalytic Water Oxidation. *ACS Nano* **2018**, *12*, 12369–12379.
- (63) Liu, K.; Wang, F.; He, P.; Shifa, T. A.; Wang, Z.; Cheng, Z.; Zhan, X.; He, J. The Role of Active Oxide Species for Electrochemical Water Oxidation on the Surface of 3d-Metal Phosphides. *Adv. Energy Mater.* **2018**, *8*, No. 1703290.
- (64) Tan, Z.; Sharma, L.; Kakkar, R.; Meng, T.; Jiang, Y.; Cao, M. Arousing the Reactive Fe Sites in Pyrite (FeS2) via Integration of Electronic Structure Reconfiguration and in Situ Electrochemical Topotactic Transformation for Highly Efficient Oxygen Evolution Reaction. *Inorg. Chem.* 2019, 58, 7615–7627.
- (65) Lin, C.; Wang, P.; Jin, H.; Zhao, J.; Chen, D.; Liu, S.; Zhang, C.; Mu, S. An Iron-Doped Cobalt Phosphide Nano-Electrocatalyst Derived from a Metal—Organic Framework for Efficient Water Splitting. *Dalt. Trans.* **2019**, *48*, 16555–16561.
- (66) McCrory, C. C. L.; Jung, S.; Ferrer, I. M.; Chatman, S. M.; Peters, J. C.; Jaramillo, T. F. Benchmarking Hydrogen Evolving Reaction and Oxygen Evolving Reaction Electrocatalysts for Solar Water Splitting Devices. *J. Am. Chem. Soc.* **2015**, *137*, 4347–4357.
- (67) Cao, L. M.; Lu, D.; Zhong, D. C.; Lu, T. B. Prussian Blue Analogues and Their Derived Nanomaterials for Electrocatalytic Water Splitting. *Coord. Chem. Rev.* **2020**, *407*, 213156.

- (68) Luo, R.; Qian, Z.; Xing, L.; Du, C.; Yin, G.; Zhao, S.; Du, L. Re-Looking into the Active Moieties of Metal X-Ides (X- = Phosph-, Sulf-, Nitr-, and Carb-) Toward Oxygen Evolution Reaction. *Adv. Funct. Mater.* **2021**, *31*, No. 2102918.
- (69) Li, H. Colloidal Cobalt Phosphide Nanocrystals as Trifunctional Electrocatalysts for Overall Water Splitting Powered by a Zinc–Air Battery. *Adv. Mater.* **2018**, *30*, No. 1705796.
- (70) Friebel, D.; W. Louie, M.; Bajdich, M.; E. Sanwald, K.; Cai, Y.; M. Wise, A.; Cheng, M.-J.; Sokaras, D.; Weng, T.-C.; Alonso-Mori, R.; C. Davis, R.; R. Bargar, J.; K. Nørskov, J.; Nilsson, A.; T. Bell, A. Identification of Highly Active Fe Sites in (Ni,Fe)OOH for Electrocatalytic Water Splitting. *J. Am. Chem. Soc.* **2015**, 137, 1305–1313.
- (71) Kresse, G.; Furthmü, J. Efficient Iterative Schemes for Ab Initio Total-Energy Calculations Using a Plane-Wave Basis Set. *Phys. Rev. B* **1996**, *54*, 16.
- (72) Kresse, G.; Hafner, J. Ab. Initio Molecular Dynamics for Liquid Metals. *Phys. Rev. B* **1993**, *47*, 558.
- (73) Perdew, J. P.; Burke, K.; Ernzerhof, M. Generalized Gradient Approximation Made Simple. *Phys. Rev. Lett.* **1997**, *78*, 1396.
- (74) Blochl, P. E. Projector Augmented-Wave Method. *Phys. Rev. B* **1994**, *50*, No. 17953.
- (75) Pack, J. D.; Monkhorst, H. J. Special Points for Brillonln-Zone Integrations"-a Reply\*. *Phys. Rev. B* **1977**, *16*, 1748.